Conical Raman-Nath nonlinear optical diffraction upon PPLN nonlinear grating

Yu Zou (邹娱)[1,†], Lihong Hong (洪丽红)[1,2,†,*], Jiacheng Li (李嘉诚)[1], Jianluo Chen (陈健洛)[1], and Zhi-Yuan Li (李志远)[1]

[1]School of Physics and Optoelectronics, South China University of Technology, Guangzhou 510641, China

[2]State Key Laboratory of Ultra-intense laser Science and Technology, Shanghai Institute of Optics and Fine Mechanics, Chinese Academy of Sciences, Shanghai 201800, China

[†]These two authors contribute equally to this work.

*Corresponding author: honglihong@siom.ac.cn

Abstract

In classical linear optics, when light shines upon a grating in the normal configuration where the incident plane of light is perpendicular to the optical axis of grating, ordinary Bragg diffraction will occur. But when light is incident in the general conical configuration where the incident plane of light is oblique to the optical axis of grating, the Bragg diffraction becomes much more complicated. What happens to nonlinear diffraction of laser beam by a nonlinear grating? In this paper we wish to answer this interesting and fundamental question in the realm of nonlinear optics. We shine a Ti:Sapphire femtosecond pulse laser beam (with central wavelength at 800 nm) upon a periodically poled lithium niobate (PPLN) thin plate nonlinear grating, and systematically investigate the Raman-Nath nonlinear diffraction (NRND) pattern of second-harmonic generation (SHG) laser beam in various “conical” (or off-plane) incidence configurations characterized by both the polar angle α and azimuthal angle φ. By analyzing the diffraction characteristic and uncovering the underlying mechanisms of conical NRND nonlinear diffraction, we have provided a comprehensive understanding of its spatial behavior. The study of conical nonlinear diffraction would enrich the understanding of complicated interaction between the pump laser beam and the structured nonlinear medium and broaden the arena of nonlinear optics.

Keywords: periodically poled lithium niobate, conical diffraction, the Raman-Nath diffraction, second-harmonic generation.

1. Introduction

As laser light propagates through a nonlinear medium, the associated electric field induces polarization within the material. This nonlinear polarization, acting as a driving source, can generate electromagnetic waves at various frequencies other than the incident pump light frequency. Typically, the induced polarization P consists of both linear and nonlinear components. The second-order nonlinear susceptibility $\chi^{(2)}$ governs phenomena such as second-harmonic generation (SHG), sum-frequency generation (SFG), and difference-frequency generation (DFG). SHG, one of the most extensively studied parametric processes in nonlinear optics, is often limited by phase mismatch due to material dispersion in nonlinear crystals. To overcome this, two widely used phase-matching techniques are birefringence phase matching (BPM)[1,2] and quasi-phase matching (QPM)[3], with the latter offering a more versatile and flexible solution to high-efficiency nonlinear frequency conversion.

QPM has been most extensively and popularly demonstrated in periodically poled lithium niobate (PPLN) and other thin plate nonlinear crystals (which cannot be very thick due to the technological limitation). QPM is commonly employed for the collinear propagation scheme of the fundamental wave (FW) and second-harmonic waves (SHW) along the modulation direction (say, x-axis) of $\chi^{(2)}$ (namely, $\chi^{(2)}(x)$) to facilitate longest coupling length and thus highest conversion efficiency[4-8]. On the other hand, when FW propagates along the z-axis (perpendicular to the modulation direction of $\chi^{(2)}(x)$) and shine upon the PPLN thin plate, fruitful nonlinear diffraction phenomena and processes, such as nonlinear Bragg diffraction (NBD)[9-12], nonlinear Cherenkov diffraction (NCR)[13-22], and nonlinear Raman-Nath diffraction (NRND)[23-32] can be generated and observed. In these situations, FW and SHW interact in a non-collinear scheme with respect to the modulation direction of the

$\chi^{(2)}$ nonlinear microstructure within the nonlinear grating[33,34]. Due to the more relaxed phase-matching conditions in the transverse direction along the reciprocal lattice vector (RLVs), NRND has garnered significant interest since its first experimental observation in 2008[23]. NRND produces multiple diffraction orders, with SHG spot emerging at various diffraction angles, analogous to the multi-order diffraction observed in linear gratings.

In nonlinear optics, the interaction between light and a medium can be manipulated by adjusting optical parameters such as the incident angle[11,20,22], the beam parameter[10], and the internal structure of the material[25,30,32]. Previous studies primarily focus on normal or oblique incidence within the vertical plane that is perpendicular to the optical axis of nonlinear grating, which is categorized as the in-plane normal incidence configuration. However, the case where the incident beam is distributed along a conical surface incorporating variations in both the polar angle α and the azimuthal angle φ, which is categorized as the off-plane conical incidence configuration, remains largely unexplored.

It is well known that in classical linear optics, when light shines upon a grating in the normal configuration where the incident plane of light is perpendicular to the optical axis of grating, ordinary Bragg diffraction will occur. But when light is incident in the general conical configuration where the incident plane of light is oblique to the optical axis of grating, the Bragg diffraction becomes much more complicated[35]. This phenomenon is known as "conical diffraction", where diffracted light rays distribute along a conical surface with the incident light direction as its axis, creating distinctive ring-shaped or arc-shaped patterns when projected onto a screen perpendicular to the optical axis[36-37]. Extending this concept to nonlinear optics, it is then interesting to ask a question: what happens to the nonlinear diffraction of laser beam by a nonlinear grating if one goes from normal incidence configuration to conical incidence configuration? Would the nonlinear diffraction pattern exhibit similar conical characteristics as observed in linear optics?

To investigate this unexplored aspect of nonlinear optical interactions and answer the above fundamental question of nonlinear diffraction, in this work we experimentally and theoretically study general conical nonlinear diffraction phenomena and physics. We shine a Ti:Sapphire femtosecond pulse laser beam (with central wavelength at 800 nm) upon a PPLN thin plate nonlinear grating, and systematically investigate the nonlinear diffraction pattern of SHG laser beam in various conical configurations characterized by both the polar angle α and azimuthal angle φ. We aim to explore the spatial distribution characteristics of NRND under conical incidence conditions, by directing a focused laser beam to obliquely incident along the generatrix of a cone onto the PPLN nonlinear crystal. These experimental and theoretical studies would enrich the fundamental understanding of conical nonlinear optical interactions and diffraction by nonlinear microstructures.

2. Models and Principles

In traditional linear diffraction experiments with gratings, the simplest situation involves observation of the diffraction phenomena against a normally incident light. This is because, under normal incidence, the diffraction angles are solely dependent on the grating period and the wavelength of the incident light, without being influenced by the incidence angle. When light is incident at a specific oblique angle, the situation becomes a little bit more complex. Yet, when light is incident at the off-plane conical configuration, things become even more complicated. Figures 1(a) and 1(c) depict the diffraction phenomena of linear dielectric gratings and PPLN nonlinear gratings under two-dimensional (2D) oblique incidence, while Figs. 1(b) and 1(d) illustrate the diffraction phenomena under conical incidence for both linear dielectric gratings and PPLN nonlinear gratings. This more complex geometrical configuration introduces unique diffraction patterns, further highlighting the distinct optical properties of PPLN compared to traditional gratings.

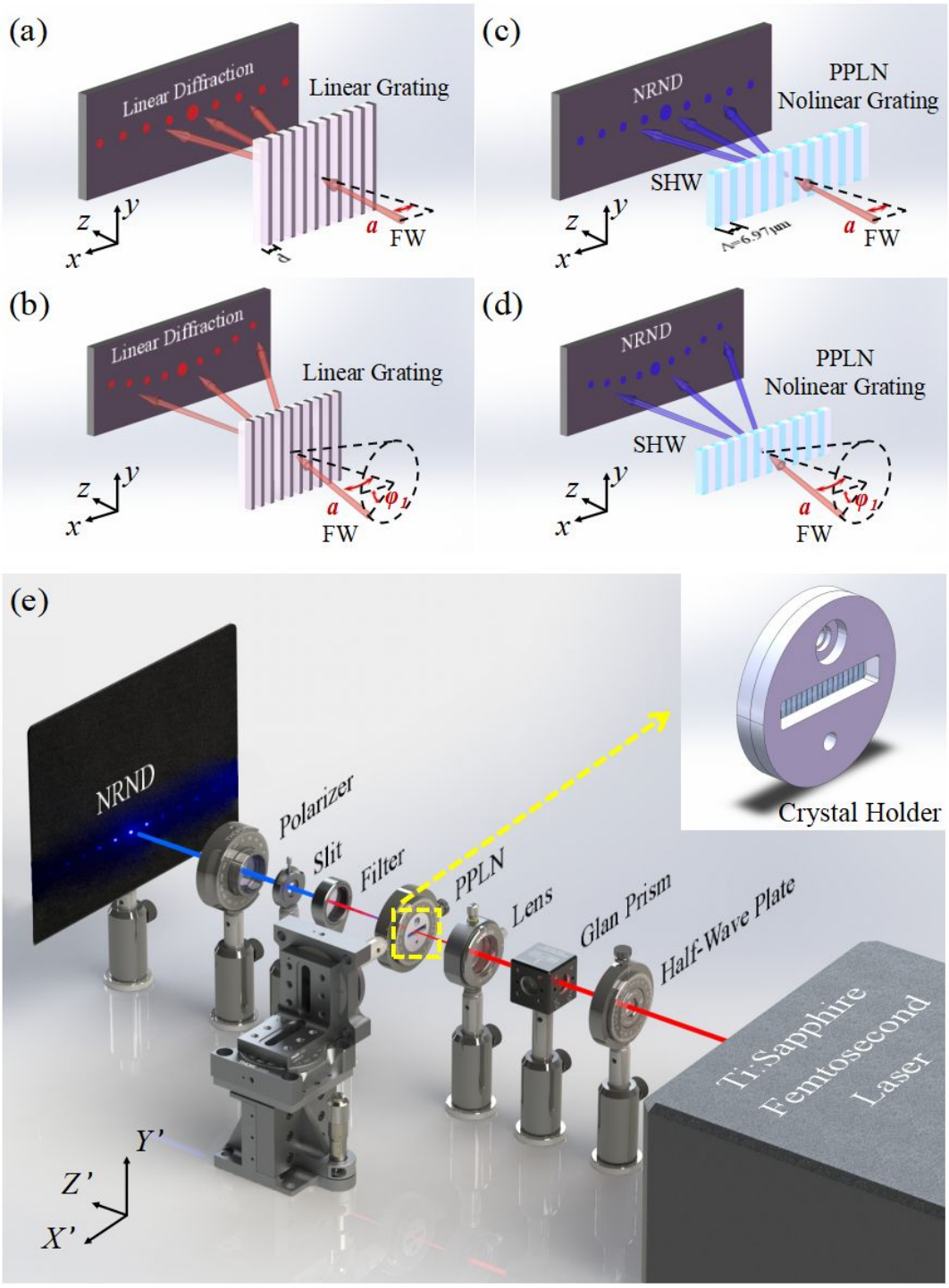

Fig. 1. Schematic scheme of linear and nonlinear diffraction in normal and conical incidence configuration. (a) Pump beam shining on a linear dielectric grating in the in-plane normal incidence configuration. (b) Pump beam shining on a linear dielectric grating in the off-plane conical incidence configuration. (c) Pump laser beam shining on a PPLN nonlinear grating in the in-plane normal incidence configuration. The poling period of the PPLN sample is 6.97 μm. (d) Pump beam shining on a PPLN nonlinear grating in the off-plane conical incidence configuration.

(e) Schematic experimental setup to study conical NRND.

We define two coordinate systems: the intrinsic crystal coordinate system (*x*-*y*-*z*) and the laboratory coordinate system (*X'*-*Y'*-*Z'*). As shown in Fig. 1(a), the grating can be analyzed along the *x* and *y* directions, with the grating lines periodically arranged along the *x*-axis and the slits extending along the *y*-axis. The incident light beam strikes the crystal at an oblique angle to the *z*-axis within the *xoz* plane, leading to variations in the distance between adjacent diffraction spots, which can be explained using the grating equation $m\lambda = d\left(\sin\alpha + \sin\beta\right)$[35], where m is the diffraction order, which can take values of 0, ±1, ±2, and so on. λ is the wavelength of the incident light, α is the incidence angle, β is the diffraction angle, and *d* is the grating period. The relative angle between the light beam and the grating determines the angular distribution of the diffracted light, with the diffraction patterns for each order distributed perpendicular to the grating lines. This figure can serve as a reference standard for subsequent conical incidence (Fig. 1(b)) and other incidence conditions.

Figure 1(b) shows the diffraction pattern when the incident light beam lies on the surface of a cone and enters the grating along its generatrix. Unlike Fig. 1(a), where the light enters in a fixed normal plane (the *xoz* plane), here the beam enters from a conical surface, with the incident direction distributed along the generatrix of the cone. Conical incidence implies that the incident beam is no longer confined to a single direction but is distributed across a 3D conical surface. This geometrical configuration results in a more complex diffraction phenomenon, with the diffraction angles not only distributed in a single plane but extending in multiple directions. This can also be described using the grating equation $m\lambda = d\left(\sin\alpha\cos\varphi_1 + \sin\beta\cos\varphi_2\right)$, where φ_1 and φ_2 represent the azimuthal angles of the incident and diffracted beams, respectively[35]. While the periodic structure of the grating still plays a role, the multidirectional nature of the incident light causes the diffraction pattern to differ

significantly from that in Fig. 1(a). Compared to Fig. 1(a) and Fig. 1(b), through conical incidence, one greatly expands the angular distribution of the incident beam, increases the diffraction angles along the *y*-axis, and the diffraction pattern takes on a more complex arc-shaped distribution. This lays the foundation for subsequent nonlinear diffraction analyses of femtosecond laser beam upon the PPLN crystal nonlinear grating in the conical incident configuration as shown in Fig. 1(d) and Fig. 1(e).

3. Experimental Setup and Sample Configuration

In the experiment, the PPLN sample we used is a *z*-cut thin plate crystal, having dimensions of 20 (*x*) mm × 5 (*y*) mm × 1 (*z*) mm and a fixed poling period Λ of 6.97 μm. In the crystal coordinate system, the origin is located at the center of the *xoy* plane of the crystal, where the *x*-axis is aligned with the modulation direction of the effective nonlinear coefficient $\chi^{(2)}(G_m)$ with a series of auxiliary RLVs[38], the *y*-axis is aligned along the domain wall extension, and the *z*-axis is aligned with the optical axis of the *z*-cut LN crystal, which is a uniaxial birefringence crystal. Similar to Fig. 1(a), the incident light beam is obliquely incident on the PPLN within the *xoz* plane. While the periodic structure of the PPLN resembles that of the grating, it is a nonlinear optical material that generates SHG diffraction through nonlinear optical effects. Its nonlinear characteristics complicate the diffraction behavior. The nonlinear nature of PPLN leads to distinct diffraction phenomena, especially at higher energies and various incidence angles, potentially resulting in intricate diffraction patterns. Figs. 1(a) and 1(c) illustrate that while both gratings and PPLN exhibit diffraction under similar incidence conditions, the diffraction beams produced by PPLN are a result of the crystal's frequency-doubling effect, and the diffraction pattern is denser than that of the grating. Unlike the oblique incidence in the *xoz* plane shown in Fig. 1(c), in Fig. 1(d), the beam also enters from a conical surface, similar to the scenario in Fig. 1(b), but the diffraction occurs in PPLN. The nonlinear optical effects in PPLN result in more pronounced curvature of the diffraction patterns compared to those

from the grating. Although both structures exhibit periodicity, the nonlinear characteristics of PPLN can lead to greater wavelength dependence in the diffraction patterns.

Due to the difficulties associated with rotating the beam and to ensure that the domain direction of the crystal (along the *x*-axis) remains parallel to the optical platform, we opted to rotate the crystal instead. This led to the experimental setup shown in Fig. 1(e). The laboratory coordinate system (*X'*-*Y'*-*Z'*) is fixed, where the *Z'*-axis is parallel to the normal incidence direction of the horizontal-propagating pump laser beam, the *Y'*-axis is perpendicular to the optical platform, and the *X'*-axis is aligned with the initial domain wall modulation direction when the crystal is placed vertical to the optical platform.

The input pump beam is a Ti:Sapphire femtosecond laser with a central wavelength of 800 nm, a pulse duration of 50 fs, a repetition rate of 1 kHz, and a pulse energy up to 4 mJ. A Glan prism is placed in the optical path to ensure that the outgoing beam is horizontally polarized (i.e., extraordinary wave against the LN crystal), with its electric field polarized parallel to the modulation direction of the poled domains, namely, the *x* axis. The laser beam is focused using a lens with a focal length of 400 mm, and the crystal is positioned just before the focus to avoid any excessive power density that could damage the crystal. At this location, the laser beam forms a 3 mm diameter spot on the crystal surface. The crystal is mounted in a crystal holder (as illustrated in the inset of Fig. 1(e)) that is embedded in a horizontal rotational adjustment stage, besides, the crystal holder can be rotated vertically. The collective rotational action of the horizontal stage and the crystal holder can generate any value of polar angle α and azimuthal angle φ_1.

When a laser beam is perpendicularly incident on the *xoy* surface of PPLN crystal, the extraordinary wave always remains parallel to the principal plane *xoz*. However, when the crystal is rotated with the beam incident at a specific angle, the extraordinary wave is no longer necessarily parallel to the principal plane *xoz*. Under these conditions, four distinct types of SHG can occur during the laser propagating

through the PPLN. The first type involves the interaction of two extraordinary waves producing an ordinary SHW [*ee-o*]; the second type results from the interaction of two extraordinary waves generating an extraordinary SHW [*ee-e*]. The third type arises from the combination of an extraordinary and an ordinary wave producing an ordinary SHW [*eo-o*], while the fourth type involves an extraordinary and an ordinary wave generating an extraordinary SHW [*eo-e*]. The tensor elements involved in these processes include d_{22}, d_{31}, and d_{33}[12,14,16,17,38]. The input power is set to 0.82W, which is well below the damage threshold of PPLN crystal. A low-pass filter below 500 nm is placed behind the PPLN crystal sample to filter out the residual fundamental signal light thereby ensuring the precise measurement of parameters related to NRND effect and the accuracy of the NRND experimental results. Since the SHG of different orders have different polarization states, a polarizer is placed after the filter to measure the power of light in both vertical and horizontal polarization directions. A flat screen is positioned 38 cm behind the crystal to receive the output NRND light spots, which is recorded using a Nikon D7200 camera.

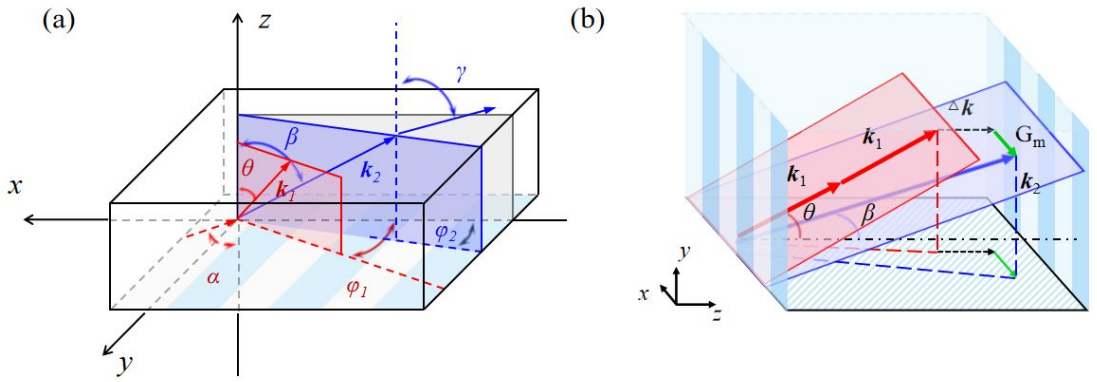

Fig. 2. (a) The three-dimensional view of the polar angles and azimuthal angles for the transmitted FW $(\theta,\ \varphi_1)$ and the generated SHW $(\beta,\ \varphi_2)$ laser beam when the pump laser beam is obliquely incident from air at an angle $(\alpha,\ \varphi_1)$ upon the PPLN nonlinear grating. k_1 and k_2 are the wave numbers of the transmitted FW laser and the generated SHW laser within the PPLN nonlinear grating, respectively. (b) Schematic illustration of the phase-matching conditions of the NRND SHG process in the PPLN crystals when the pump laser beam obliquely

incident upon the PPLN nonlinear grating.

Figure 2(a) illustrates the schematic of the beam path of the incident FW and the generated SHW. We suppose the incident beam enters the PPLN nonlinear grating from air at a certain conic angle of $(\alpha,\ \varphi_1)$, where α is the incident polar angle with respect to the *z*-axis and φ_1 is the azimuthal angle with respect to the *x*-axis, both measured in the air side. It undergoes refraction within the crystal due to the interfacial refraction law of light, resulting in a refraction polar and azimuthal angle $(\theta,\ \varphi_1)$, which will totally determine the transmitted FW wave transport features together with the FW wave vector k_1 (denoted in red plane in Fig. 2(a)) within the LN crystal. When the interaction between FW and PPLN crystal occurs, a SHW is generated with a wave number k_2 and propagates in a distinct plane (shown in blue plane in Fig. 2(a)), differing from the FW's red plane. We define the SHG angular coordinates as $(\beta,\ \varphi_2)$, where β is the angle between the SHW and the optical axis, and φ_2 is the azimuthal angle in the *xoy* plane relative to the *x*-axis. Both the polar and azimuthal angles of the SHW differ from those of the FW. Similarly, following Snell's law, when the SHW propagates to the rear surface of the crystal and exits into the air, the propagation can be characterized by the refraction angle of $(\gamma,\ \varphi_2)$, where γ is the angle between the external SHW and the optical axis of the crystal.

To provide a clearer understanding of this conical nonlinear diffraction process with the PPLN slab, we construct and analyze the 3D physical diagram of NRND QPM conditions, as presented in Fig. 2(b). Obviously, the general vector phase-matching condition, $2\boldsymbol{k}_1 + G_m + \Delta k = \boldsymbol{k}_2$, holds under various incident conditions. We readily find the phase matching components along the *x*-axis, *y*-axis, *z*-axis within the PPLN thin plate satisfies the geometric configuration defined by

$$
\begin{aligned}
k_{2x} &= 2k_1 \sin\theta\cos\varphi_1 - k_2(\lambda_2)\sin\beta\cos\varphi_2 = G_m, \quad m = 0, \pm 1, \pm 2\mathrm{K} \\
k_{2y} &= k_2(\lambda_2)\sin\beta\sin\varphi_2 = 2k_1\sin\theta\sin\varphi_1, \\
k_{2z} &= k_2(\lambda_2)\cos\beta = 2k_1\cos\theta + \Delta k,
\end{aligned} \tag{1}
$$

where $k_2 = \dfrac{2\pi n_2}{\lambda_2}$ represents the SHW signal's wave vector, $G_m = \dfrac{2\pi m}{\Lambda}$ is the reciprocal lattice vector, m is NRND order, and Λ is the poling period of the PPLN crystal (6.97 μm). Δk represents the phase mismatch along the z-axis. By solving the phase-matching equations, we can determine the SHW beam's angle β with respect to the z-axis, as well as the projection angle φ_2 in the xoy plane, which are

$$
\beta = \arcsin\left(\sqrt{\left(\frac{\sin\alpha}{n_2}\right)^2 - \frac{2\sin\alpha m\lambda_2}{\Lambda n_2^2}\cos\varphi_1 + \left(\frac{m\lambda_2}{n_2\Lambda}\right)^2}\right), \tag{2}
$$

$$
\varphi_2 = \arctan\left(\frac{2\sin\alpha\sin\varphi_1\Lambda}{2\sin\alpha\cos\varphi_1\Lambda - m\lambda_1}\right). \tag{3}
$$

By using the Snell's law described by $\sin\gamma = n_2(\beta, \varphi_2)\sin\beta$, we find that the external polar angle of SHW in the air is

$$
\gamma = \arcsin\left(\sqrt{(\sin\alpha)^2 - \frac{2m\lambda_2\sin\alpha}{\Lambda}\cos\varphi_1 + \left(\frac{m\lambda_2}{\Lambda}\right)^2}\right). \tag{4}
$$

Equations (3) and (4) clearly reveal that change in the incident angle α and azimuthal angle φ_1 of FW beam, the wavelength λ of the interacting waves, the diffraction order m, and the poling period Λ of PPLN, would result in corresponding changes in the exit angles γ and φ_2 of SHW. Notably, γ, which is the angle between the SHW beam in air and the crystal's z-axis, is independent of the refractive index n_2 of the SHW beam within the crystal. This indicates that the emission angle of the SHW beam is unaffected by both its polarization state and refractive index.

4. Experimental Results and Discussion

Figures 3(a) to 3(d) illustrate the geometric diagram of the PPLN crystal rotation and

the generated NRND spots observed in experiment, where the pump beam consistently propagates along the Z'-axis in the laboratory frame. In this experiment, the laser pulse energy was set at 0.82 W, with a duration of 50 fs, and the beam diameter incident on the front surface of the crystal was approximately 3 mm. The diffraction screen was positioned 38 cm behind the PPLN crystal, allowing for the clear observation of the NRND diffraction pattern generated by the crystal on the screen. These parameters ensured the reproducibility and consistency of the experimental results, providing a reliable basis for the analysis of the observed diffraction patterns.

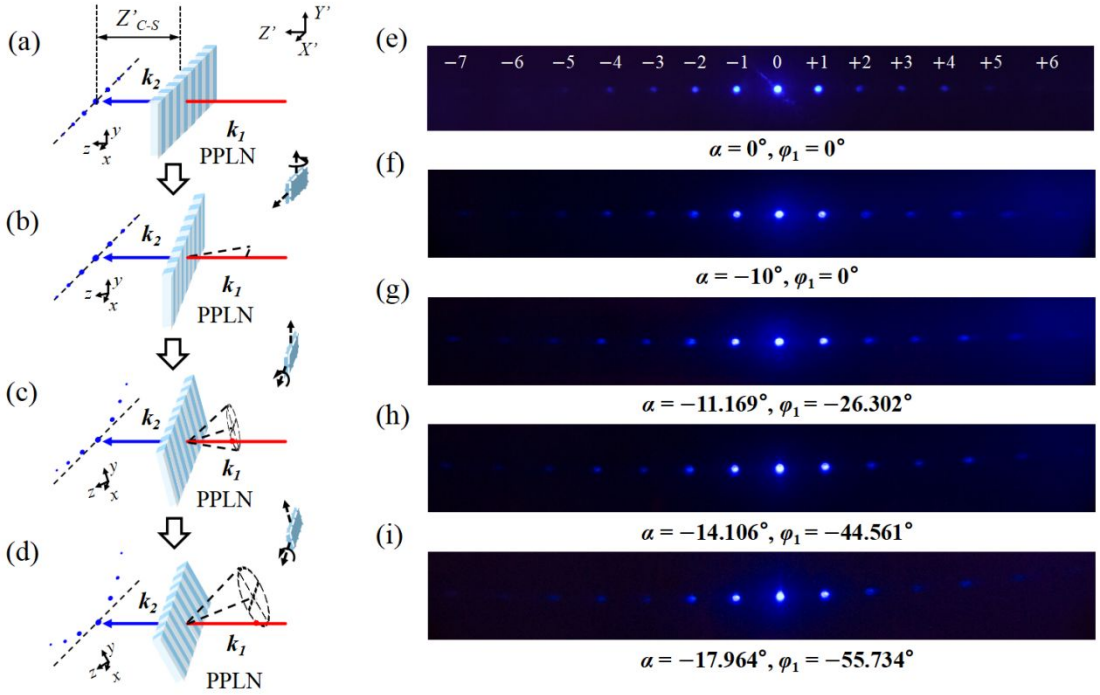

Fig. 3. (a)-(d) Schematic illustration showing NRND phenomena at various cone-angle incidence by rotating the PPLN thin plate but keeping the pump laser beam incident along the Z'-axis of laboratory coordinate system. (e)-(i) Experimental NRND patterns at different conical incidence. $Z'_{C\text{-}S}$ is the distance between the crystal and the detection screen.

Figures 3(e) to 3(i) presents the experimental results under varying incident angles. From top to bottom, the incident angles are: $\alpha = 0°,\ \varphi_1 = 0°$; $\alpha = -10°,\ \varphi_1 = 0°$; $\alpha = -11.169°,\ \varphi_1 = -26.302°$; $\alpha = -14.106°,\ \varphi_1 = -44.561°$; and

$\alpha = -17.964°$, $\varphi_1 = -55.734°$. Here, negative angles are defined as follows: when viewed from the negative *z*-axis, the polar angle α is defined as the negative angle formed by the incident beam rotating from the *yoz* plane towards the positive *x*-axis. Similarly, the azimuthal angle φ_1 is characterized as the negative angle formed by the incident beam rotating from the *xoz* plane towards the negative *y*-axis. Consequently, when both α and φ_1 are negative, the beam resides in the eighth quadrant of the crystal coordinate system.

Figure 3(a) shows the case of normal beam incidence, corresponding to the experimental result in Fig. 3(e), where $\alpha = 0°$, $\varphi_1 = 0°$. The observed and recorded diffraction spots correspond to seven nonlinear diffraction orders on the left and six on the right of the central spot, defining negative orders on the left and positive orders on the right. Overall, the emitted diffraction spots keep at the same horizontal coordinate line (parallel to the *x*-axis) in this case. Moving from Fig. 3(a) to 3(b), the PPLN crystal is rotated about the *y*-axis by an angle α, thus introducing a polar angle α. Here, a counterclockwise rotation of 10° around the *y*-axis results in the beam rotating clockwise relative to the *yoz* plane, giving a result of $\alpha = -10°$, as reflected in Fig. 3(f). On this condition, the NRND spots still keep at the same horizontal coordinate line but with slightly larger diffraction angle. Subsequently, from Fig. 3(b) and 3(c), the crystal is rotated about the *x*-axis by an angle φ_1, introducing an azimuthal angle φ_1. A 5° counterclockwise rotation around the *x*-axis causes the beam to rotate clockwise relative to the *xoz* plane. Using the angle transformation formula, this results in $\alpha = -11.169°$, $\varphi_1 = -26.302°$. At these stages, both the azimuthal angle and the half-cone angle have changed, which can be calculated from formulas $\alpha = -\arccos\left[\cos\left(y_{rotate}\right)\cos\left(x_{rotate}\right)\right]$ and $\varphi_1 = -\arctan\left[\cot\left(y_{rotate}\right)\sin\left(x_{rotate}\right)\right]$, where x_{rotate} and y_{rotate} represent the rotation angle with respect to the *x* and *y*-axis. The corresponding experimental result in Fig. 3(g) shows that the diffraction spots no longer align horizontally and begin to deviate

away in the vertical direction (namely the *z*-axis).

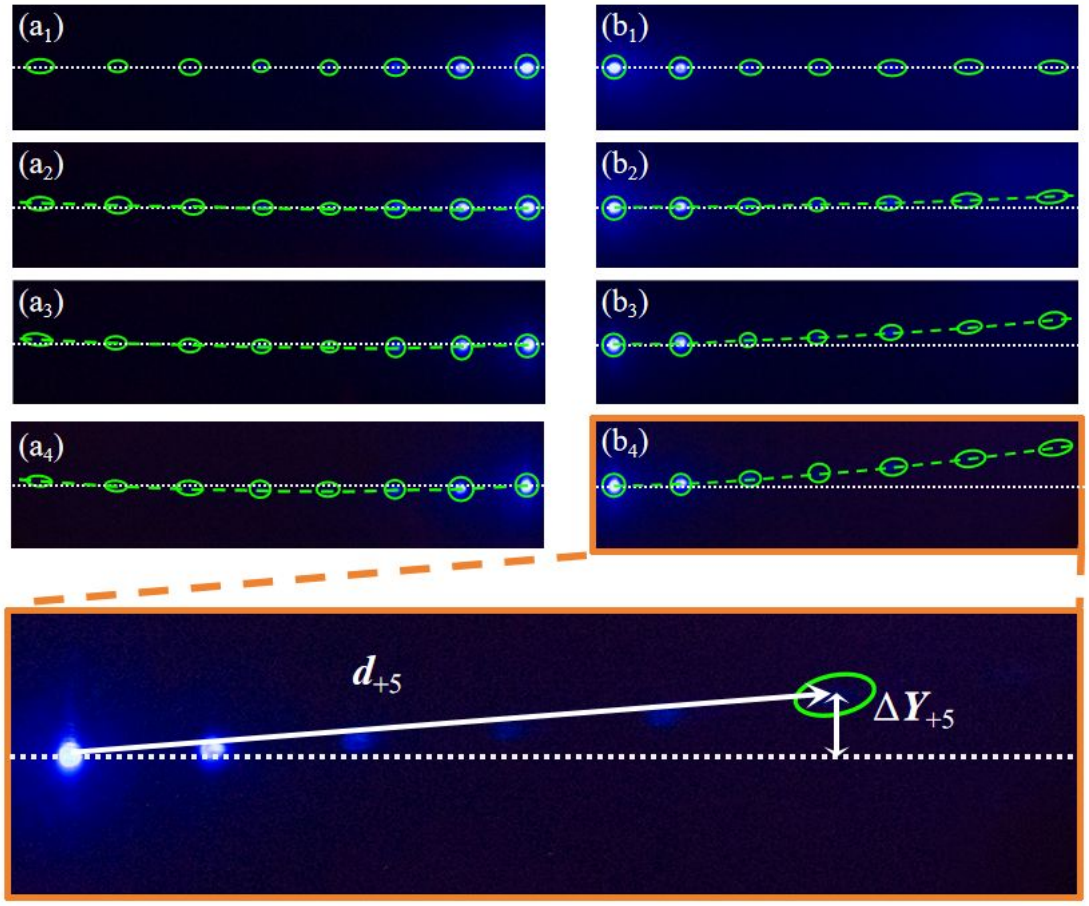

Fig. 4. Enlarged image of the experimental NRND patterns at different cone angles of incidence. For the distribution lines of diffraction points on the left and right sides, the green dashed line is the line connecting each order, and the white dashed line is the horizontal line relative to the laboratory coordinate system where the m=0 order is located. (a_1)-(a_4) NRND spots located to left-hand sides of the central spot under different incident angles (defined as negative diffraction orders). (b_1)-(b_4) NRND spots located to right-hand sides of the central spot under different incident angles (defined as positive diffraction orders). Inset: expanded view of (b_4). ΔY is the deviation of each order of diffracted spot from the horizontal line of the m=0 order in the Y'-axis of laboratory coordinate system, while d is the distance between each order of diffracted spot and the m=0 order.

As the crystal continues to rotate around the *x*-axis (from Figs. 3(c) to 3(d)), the absolute values of both the azimuthal angle φ_1 and the polar angle α increase. This indicates that the cone angle of the beam's conical surface is widening, as

observed in the experimental results in Figs. 3(h) and 3(i). The diffraction pattern takes on an irregular, arc-shaped arrangement, and as the cone angle increases, the curvature of the arc formed by the diffraction spots also increases. The distribution of the diffraction orders is asymmetric relative to the central diffraction spot, with the diffraction spots on the right shifting towards the positive *Y'*-axis. As the diffraction order increases, the distance between the higher-order spots and the 0th-order spot in the *Y'* direction grows. In contrast, the diffraction spots on the left deviate less dramatically than those on the right. The asymmetry can be well explained by Eqs. (3) and (4). As derived from Eqs. (3) and (4), when the pump laser beam is incident at an angle, the exit angles γ and azimuthal angles φ_2 for each diffraction order differ, and the principal planes of the diffraction orders are no longer the same. Furthermore, due to differences at the diffraction orders of emitted beam, the spots show deviations in the *Y'*-direction, thus forming a conical arc-like arrangement of diffraction patterns.

To better visualize and quantify the distribution characteristics of NRND spots across different incident angles, the diffraction spots at different orders are connected by green dashed lines, as illustrated in Figs. 4(a_1) to 4(b_4), again clearly revealing an increasing conical curvature from top panel to bottom panel. Experimentally, the NRND diffraction angles σ_m=arctan$\left(d / Z'_{C-S}\right)$ are determined by measuring the distance between the crystal and the detection screen, defined as Z'_{C-S} (as indicated in Fig. 3(a)), along with the separation *d* between the diffraction spots of each order and the 0th-order spot on the screen. This angle can be theoretically calculated using the formula $\cos\sigma_m = (\boldsymbol{k}_{20} \cdot \boldsymbol{k}_{2m}) / (|k_{20}||k_{2m}|)$, and we find

$$\sigma_m = \arccos\left(\sin\alpha\cos\varphi_1 \sin\gamma\cos\varphi_2 + \sin\alpha\sin\varphi_1\sin\gamma\sin\varphi_2 + \cos\alpha\cos\gamma\right). \quad (5)$$

Here one can find that the deviation is influenced by both the incident FW orientation angles of $(\alpha,\ \varphi_1)$ and the output SHW orientation angles of $(\gamma,\ \varphi_2)$. A comparison of the experimental and theoretical diffraction angles is shown in Fig. 5. The data show a strong consistence between the experimental measurements and

theoretical predictions. The changes in the incident angles α and φ_1 lead to slight differences in the output diffraction angles. Notably, the angular distribution exhibits a non-symmetric pattern between the positive and negative diffraction orders. This asymmetry points to potential new insights into the interaction between incident light and the crystal structure under such a special conical pump configuration.

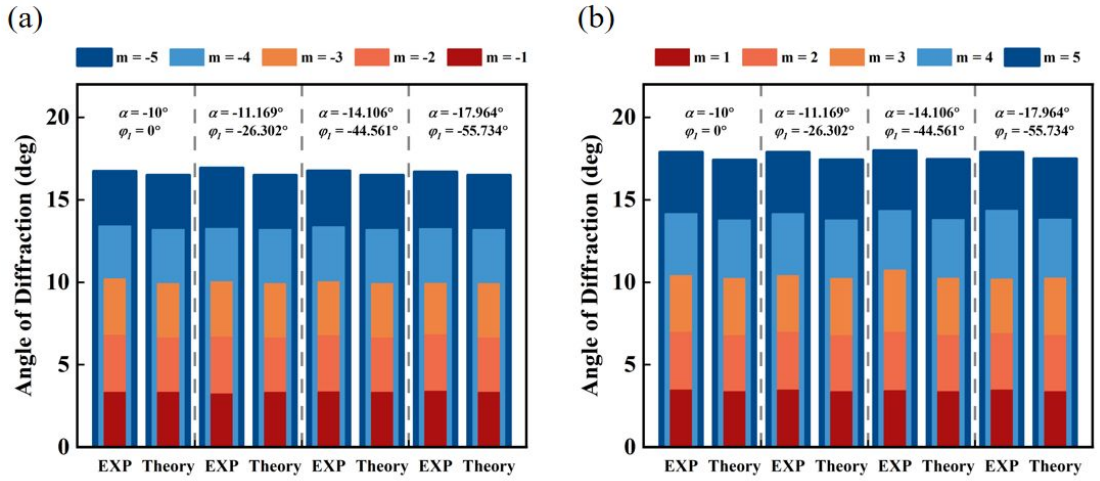

Fig. 5. Theoretical and experimental comparison of the diffraction angular distribution between multiple-order NRND diffraction spots and *m*=0 order diffraction spot under various cone-angle incidences. A series of ordered NRND spots that correspond to the five nonlinear diffraction orders, including $|m|=1$ (red), $|m|=2$ (orange), $|m|=3$ (yellow), $|m|=4$ (wathet), $|m|=5$ (dark blue) in the neighborhood of the transmitted fundamental laser spot. (a) Negative NRND diffraction spots located to left-hand sides of the central spot. (b) Positive NRND diffraction spots located to right-hand sides of the central spot.

Further, we introduce a deviation angle to describe the degree of the arc-shaped arrangement of the diffraction spots for various incident angles, which is defined as the angle between each diffraction order and the 0th-order output beam, named as $\psi_m = \arctan\left(\Delta Y / Z'_{C-S}\right)$. Experimentally, the deviation angle ψ_m is determined by measuring the distance between the crystal and the detection screen Z'_{C-S}, as well as the vertical displacement ΔY between the diffraction spots of each order and the horizontal line passing through the 0th-order spot on the screen. These parameters are

clearly illustrated in the inset of Fig. 4(b_4). To facilitate a more intuitive observation and explanation of this diffraction angle deviation phenomenon, we have made a comparison between theoretical predictions and experimental measurements and show the result in Fig. 6.

In the absence of the azimuthal angle, namely $\varphi_1 = 0$, all diffraction spots align on the same horizontal straight line, resulting in a deviation angle being exactly $0°$. However, when the azimuthal angle φ_1 is present, we can examine the deviation angles numerically, and the results are shown in Figs. 6(b)-(d). Here, we define the 0th-order horizontal line as $0°$, with the diffraction spots located below this line yielding negative deviation values, and those above this line yielding positive values.

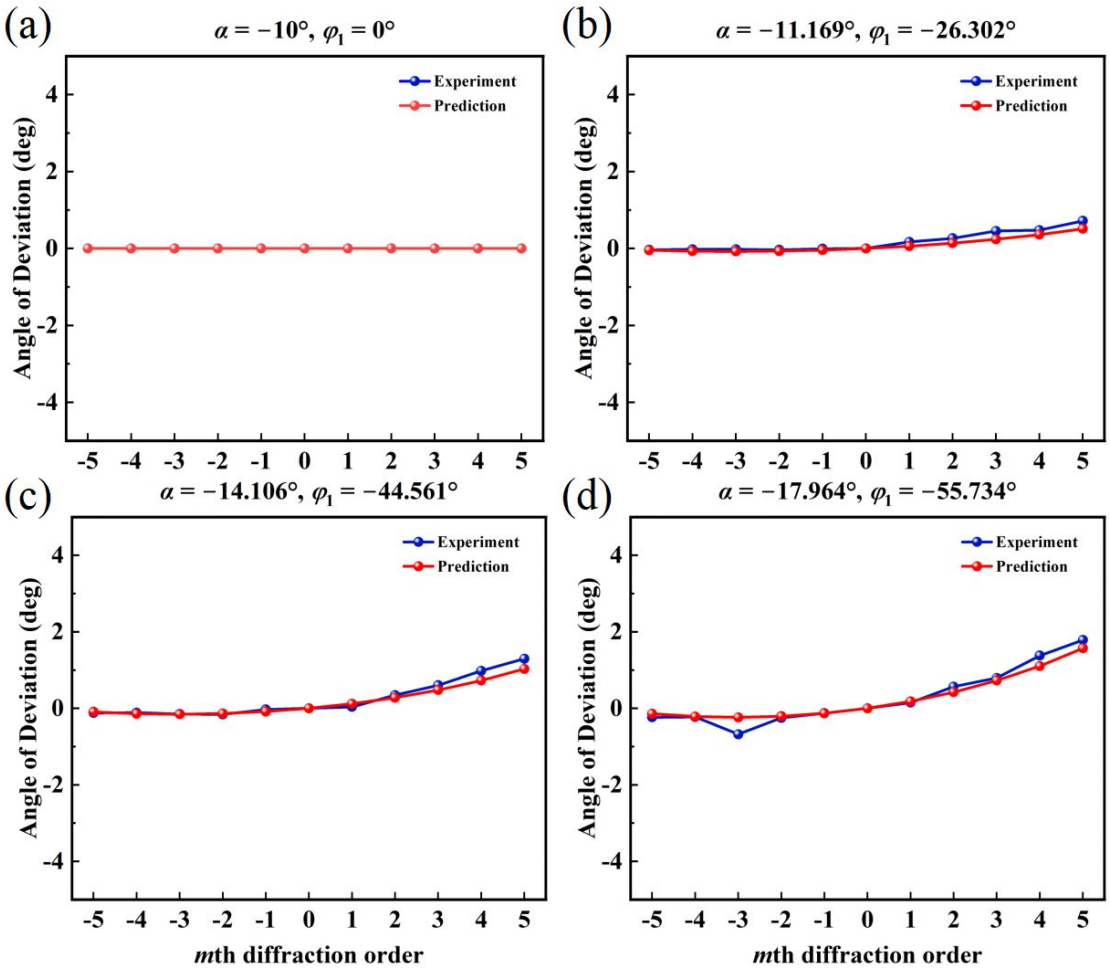

Fig. 6. Analysis of the deviation angle ψ_m of NRND diffracted spots at different diffraction orders from the horizontal line of the m=0 order along the Y'-axis of laboratory coordinate system

with different incident angles. (a) $\alpha = -10°,\ \varphi_1 = 0°$; (b) $\alpha = -11.169°,\ \varphi_1 = -26.302°$; (c) $\alpha = -14.106°,\ \varphi_1 = -44.561°$; (d) $\alpha = -17.964°,\ \varphi_1 = -55.734°$.

Figure 6(c)-(d) all reveal that as the diffraction order increases, the deviation angle on the right side of the central spot gradually increases, revealing increasingly significant cone-angle radiation characteristics. In contrast, the deviation angle on the left side exhibits a more complex behavior. As shown in Fig. 6(d), during the variation from the 0th-order to the -5-order, the deviation angle ψ_m initially increases and then decreases along the -*Y'* direction. This results visually indicates that NRND effect does not exhibit a linear conical influence on the radiated directions of different diffraction orders under specific cone angle incidence conditions. The theoretical and experimental analyses reveal minor discrepancies, which may stem from insufficient precision in measuring the size and position of the diffraction spots.

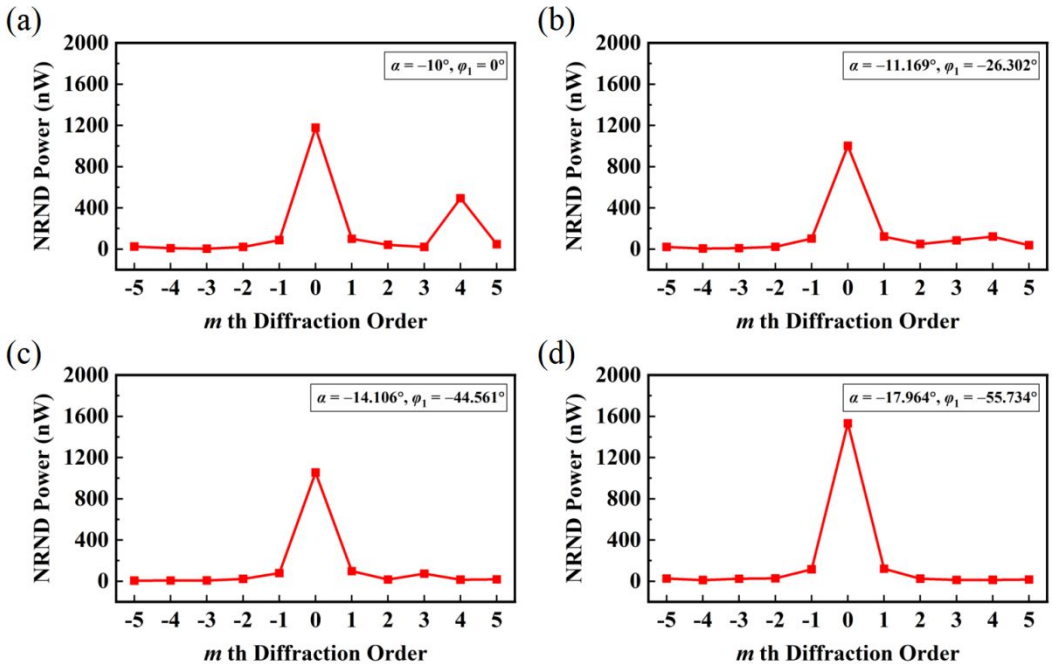

Fig. 7. Analysis of the diffraction spots power of different NRND diffraction orders generated by the pump light passing through PPLN at different incidence angles. (a) $\alpha = -10°,\ \varphi_1 = 0°$; (b) $\alpha = -11.169°,\ \varphi_1 = -26.302°$; (c) $\alpha = -14.106°,\ \varphi_1 = -44.561°$; (d)

$\alpha = -17.964°,\ \varphi_1 = -55.734°$.

Finally, we present the diffraction power of each diffraction SHG beam at different incident angles using a line graph. A suitable low-pass filter is selected and placed before the power meter to eliminate any residual pump light energy, ensuring that the power meter probe remains perpendicular to each diffracted beam. Due to the phase mismatch in the longitudinal direction (*z*-direction), the conversion efficiency of this process is relatively low, with only a small fraction of the FW pump light being converted to NRND SHG beam. The measured power levels are illustrated in Fig. 7. As illustrated in Figs. 7(a) to 7(d), for every incident angle, the 0th-order diffraction exhibits relatively higher power, while higher-order diffractions show progressively weaker power, following a decreasing trend consistent with typical energy distribution in diffraction processes. Despite variations in the incident angle, the nW-level powers can still be accurately measured, and the variations in power for the same diffraction order are not significant. Further analysis of the energy distribution across various diffraction orders reveals that, although power variations between the orders are minimal, distinct energy differences still exist between the diffraction orders. Although the overall diffraction power is not particularly high, it nonetheless effectively reflects the nonlinear optical properties of the PPLN crystal.

5. Conclusion

In summary, we have realized the conical NRND in a single PPLN nonlinear grating shined by a high-peak-power Ti:Sapphire femtosecond pump laser with different incident polar angels and azimuthal angles. To comprehensively validate the diffraction characteristics under this general conical incidence configuration of pump laser, we investigate the angular distribution of SHG across different diffraction orders including both the diffraction and deviation angles. We further measure the NRND power and polarization angles for different diffraction orders in PPLN crystals. The experimental findings reveal that, as the conical incidence angle increases, the 0th-order beam remains collinear with the incident beam, while the

diffraction spots at different spots located on the both sides of the central diffraction spot follow by a curved trajectory, with the curvature of the trajectory becoming more pronounced at larger incident conical angles.

In the context of conical NRND, transverse phase matching exhibits significant angular tuning flexibility due to introducing the physical parameters of polar angels and azimuthal angles. This novel approach of conical incidence provides profound insights into the physical mechanisms underlying NRND in nonlinear optical microstructures, offering enhanced control over ultrashort pulse laser interactions in nonlinear media. The conical tuning technique greatly increases the degrees of freedom for NRND TPM control in nonlinear crystals. We anticipate that this method would lead to advanced techniques for ultrashort pulse characterization, high-precision distortion measurement of domain structures and beam collimation diagnostics, thereby providing promising and powerful tools for nonlinear optical systems and metrology.

Acknowledgments. We acknowledge the financial support from Science and Technology Project of Guangdong (2020B010190001), National Natural Science Foundation of China (12434016), and National Funded Postdoctoral Researcher Program (GZB20240785).

Disclosures. The authors declare no conflicts of interest.

Data Availability. Data underlying the results presented in this paper are not publicly available at this time but may be obtained from the authors upon reasonable request.

References

1. P. A. Franken and J. F. Ward, “Optical Harmonics and Nonlinear Phenomena,” Rev. Mod. Phys. **35**, 23 (1963).
2. W. N. Herman and L. M. Hayden, “Maker fringes revisited: second-harmonic generation

from birefringent or absorbing materials," J. Opt. Soc. Am. B **12**, 416 (1995).

3. M. M. Fejer, G. A. Magel, D. H. Jundt, *et al.*, "Quasi-phase-matched second harmonic generation: tuning and tolerances," IEEE J. Quantum Elect. **28**, 2631 (1992).
4. B. Q. Chen, M. L. Ren, R. J. Liu, *et al.*, "Simultaneous Broadband Second and Third Harmonic Generation in Chirped Nonlinear Photonic Crystal," Light-Sci. Appl. **3**, e189 (2014).
5. B. Q. Chen, C. Zhang, C. Y. Hu, *et al.*, "High-Efficiency Broadband High-Harmonic Generation from a Single Quasi-Phase-Matching Nonlinear Crystal," Phys. Rev. Lett. **115**, 083902 (2015).
6. B. Q. Chen, L. H. Hong, C. Y. Hu, *et al.*, "White laser realized via synergic second- and third-order nonlinearities," Research **2021**, 1539730 (2021).
7. L. H. Hong, H. Y. Yang, L. Q. Liu, *et al.*, "Intense and superflat white laser with 700 nm 3 dB bandwidth and 1 mJ pulse energy enabling single-shot femtosecond-pulse-laser spectroscopy," Research, **6**, 0210 (2023).
8. L. H. Hong, L. Q. Liu, Y. Y. Liu, *et al.*, "Intense ultraviolet-visible-infrared full-spectrum laser," Light: Sci. Appl. **12**, 199 (2023).
9. I. Freund, "Nonlinear diffraction," Phys. Rev. Lett. **21**, 1404 (1968).
10. A. M. Vyunishev, V. G. Arkhipkin, I. S. Baturin, *et al.*, "Multiple nonlinear Bragg diffraction of femtosecond laser pulses in a photonic lattice with hexagonal domains," Laser Phys. Lett. **15**, 045401 (2018).
11. S. M. Saltiel, D. N. Neshev, W. Krolikowski, *et al.*, "Multiorder nonlinear diffraction in frequency doubling processes," Opt. Lett. **34**, 848 (2009).
12. S. M. Saltiel, D. N. Neshev, R. Fischer, *et al.*, "Generation of Second-HarmonicConical Waves via Nonlinear Bragg Diffraction," Phys. Rev. Lett. **100**, 103902 (2008).
13. Y. Zhang, Z. D. Gao, Z. Qi, *et al.*, "Nonlinear Cerenkov Radiation in Nonlinear Photonic Crystal Waveguides," Phys. Rev. Lett. **100**, 163904 (2008).
14. S. M. Saltiel, Y. Sheng, N. V. Bloch, *et al.*, "Cerenkov-type second-harmonic generation in two-dimensional nonlinear photonic structures," IEEE J. Quantum Elect. **45**, 1465 (2009).
15. Y. Zhang, X. P. Hu, G. Zhao, *et al.*, "Cerenkov second-harmonic arc from a hexagonally poled $LiTaO_3$ planar waveguide," J. Phys. D: Appl. Phys. **42**, 215103 (2009).

16. Y. Sheng, S. M. Saltiel, W. Krolikowski, *et al.*, "Cerenkov-type second-harmonic generation with fundamental beams of different polarizations," Opt. Lett. **35**, 1317 (2010).
17. P. Molina, M. O. Ramírez, B. J. García, *et al.*, "Directional dependence of the second harmonic response in two-dimensional nonlinear photonic crystals," Appl. Phys. Lett. **96**, 261111 (2010).
18. A. M. Vyunishev, A. S. Aleksandrovsky, A. I. Zaitsev, *et al.*, "Čerenkov nonlinear diffraction of femtosecond pulses," J. Opt. Soc. Am. B **30**, 2014 (2013).
19. L. H. Hong, B. Q. Chen, C. Y. Hu, *et al.*, "Rainbow Cherenkov second-harmonic radiation," Phys. Rev. Appl. **18**, 044063 (2022).
20. S. M. Saltiel, D. N. Neshev, W. Krolikowski, *et al.*, "Nonlinear diffraction from a virtual beam," Phys. Rev. Lett. **104**, 083902 (2010).
21. A. Shapira and A. Arie, "Phase-matched nonlinear diffraction," Opt. Lett. **36**, 1933 (2011).
22. K. Kalinowski, P. Roedig, Y. Sheng, *et al.*, "Enhanced Čerenkov second-harmonic emission in nonlinear photonic structures," Opt. Lett. **37**, 1832 (2012).
23. S. M. Saltiel, D. N. Neshev, R. Fischer, *et al.*, "Generation of second-harmonic Bessel beams by transverse phase-matching in annular periodically poled structures," Jap. J. Appl. Phys. **47**, 6777 (2008).
24. Y. Sheng, Q. Kong, W. J. Wang, *et al.*, "Theoretical investigations of nonlinear Raman-Nath diffraction in the frequency doubling process," J. Phys. B: Atom. Mol. Opt. Phys. **45**, 055401 (2012).
25. N. V. Bloch, K. Shemer, A. Shapira, *et al.*, "Twisting light by nonlinear photonic crystals," Phys. Rev. Lett. **108**, 233902 (2012).
26. Y. Chen, W. Dang, Y. Zheng, *et al.*, "Spatial modulation of second-harmonic generation via nonlinear Raman-Nath diffraction in an aperiodically poled lithium tantalite," Opt. Lett. **38**, 2298 (2013).
27. A. M. Vyunishev, V. V. Slabko, I. S. Baturin, *et al.*, "Nonlinear Raman-Nath diffraction of femtosecond laser pulses," Opt. Lett. **39**, 4231 (2014).
28. H. G. Liu, J. Li, X. H. Zhao, *et al.*, "Nonlinear Raman-Nath second harmonic generation withstructured fundamental wave," Opt. Express **24**, 15666 (2016).
29. H. Q. Zhou, H. G. Liu, M. H. Sang, *et al.*, "Nonlinear Raman-Nath second harmonic

generation of hybridstructured fundamental wave," Opt. Express **25**, 3774 (2017).

30. D. A. Ikonnikov, V. G. Arkhipkin, and A. M. Vyunishev, "Controlling multiple diffraction with quasiperiodic gratings," Laser Phys. Lett. **16**, 126202 (2019).
31. Y. Chen, Y. Liu, R. Zhao, *et al.*, "Second-Harmonic Generation via Nonlinear Raman-Nath Diffraction in an Optical Fibonacci Superlattice," Cryst. Res. Technol. **57**, 2100193 (2022).
32. L. H. Hong, B. Q. Chen, C. Y. Hu, *et al.*, "Ultrabroadband nonlinear Raman-Nath diffraction against femtosecond pulse laser," Photonics Res. **10**, 905 (2022).
33. R. Fischer, S. M. Saltiel, D. N. Neshev, *et al.*, "Broadband femtosecond frequency doubling in random media," Appl. Phys. Lett. **89**, 191105 (2006).
34. S. Saltiel, W. Krolikowski, D. Neshev, *et al.*, "Generation of Bessel beams by parametric frequency doubling in annular nonlinear periodic structures," Opt. Express **15**, 4132 (2007).
35. J. E. Harvey and C. L. Vernold, "Description of diffraction grating behavior in direction cosine space," Appl. Opt. **37**, 8158 (1998).
36. Y. J. Liu, W. Q. Li, Q. X. Ding, *et al.*, "Total internal reflection diffraction grating in conical mounting and its application in planar display," Proc. SPIE: *The International Conference on Photonics and Optical Engineering* (*icPOE* 2014) **9449**, 324 (2015).
37. J. E. Harvey and R. N. Pfisterer, "Understanding diffraction grating behavior: including conical diffraction and Rayleigh anomalies from transmission gratings," Opt. Eng. **58**, 087105 (2019).
38. L. H. Hong, Y. Zou, J. C. Li, *et al.*, "Unified analytical theory of nonlinear optical diffraction by nonlinear gratings," J. Opt. Soc. Am. B, **41**, 2562 (2024).